Journal of Catalysis 396 (2021) 32–39

Contents lists available at ScienceDirect

Journal of Catalysis

journal homepage: www.elsevier.com/locate/jcat

In-operando surface-sensitive probing of electrochemical reactions on nanoparticle electrocatalysts: Spectroscopic characterization of reaction intermediates and elementary steps of oxygen reduction reaction on Pt

Sean T. Dix [a,b], Suljo Linic [a,b,*]

[a] Department of Chemical Engineering, University of Michigan, Ann Arbor, MI, USA
[b] Michigan Catalysis Science and Technology Institute (MiCSTI), University of Michigan, Ann Arbor, MI, USA

ARTICLE INFO

Article history:
Received 4 December 2020
Revised 11 January 2021
Accepted 7 February 2021
Available online 17 February 2021

Keywords:
Electro-catalysis
ORR
Mechanism
SERS
Intermediates

ABSTRACT

In this paper we present an in-operando spectroscopic study of the reaction intermediates involved in ORR on electrified Pt nanoparticle electrocatalysts. To accomplish this, we have synthesized Ag-Pt core–shell nanoparticles, that contain a thin shell of Pt (~1 nm) uniformly deposited on a larger Ag core (~60 nm). We show that these nanostructures are ideal platforms for in-operando Plasmon Enhanced Raman Spectroscopy (PERS) of ORR on Pt. We combined these PERS studies with DFT calculations to assign the measured vibrational spectra to relevant surface intermediates as a function of electrocatalyst potential. These vibrational assignments were further verified and validated by performing PERS measurements using de-oxygenated and heavy oxygen (O_2-18) saturated electrolyte. These studies allowed us to identity the presence of critical reaction intermediates (OH, O_2, OOH, and H_2O) as the function of operating voltage on the Pt surface and derive voltage-dependent elementary step mechanisms of the reaction.

1. Introduction

Hydrogen fuel cells take advantage of two electrochemical half reactions, hydrogen oxidation (HOR) at the anode and oxygen reduction (ORR) at the cathode, to exchange chemical for electrical energy [1–3]. Owing largely to the sluggish kinetics of the cathodic ORR even on state-of-the-art Pt-based nanoparticle electrocatalysts, these devices have not enjoyed a widespread adoption [4,5]. To combat this issue, there have been many attempts to improve the electrocatalyst efficiency by combining Pt with other metals to form Pt-metal alloys that exhibit higher reaction rates compared to pure Pt materials [6–9]. These studies have yielded a number of promising ORR electrocatalysts, among which Pt/3d (Ni, Co, Cu) metal alloy nanoparticles show the most promise [10–15].

Parallel to these efforts to identify better performing ORR electrocatalysts, there has also been a significant interest to unearth the reaction mechanism at the elementary step and critical surface intermediates levels [16–22]. Obtaining direct experimental spectroscopic evidence, in the form of vibrational or electronic spectra of relevant ORR surface intermediates at the electrified interfaces between an electrolyte and Pt nanoparticle electrocatalysts, however, has proven challenging. The experimental difficulties are associated with (i) the lack of surface sensitivity of many spectroscopic techniques, making it difficult to separate the spectroscopic signals associated with surface reaction intermediates from those associated with the species in the water-based electrolyte [23], (ii) the presence of the interfacial electric field effects which change as the electrode potential changes, (iii) the presence of water molecules whose interfacial surface orientation changes as a function of potential, and (iv) the existence of electrolyte ions which further complicate the mechanism [24–29]. Due to these difficulties, spectroscopic studies of ORR have been rather limited and mainly focused on highly idealized model electrocatalysts or on idealized electrochemical environments that are not consistent with the above described electrocatalyst/electrolyte interface complexities [30]. For example, Adzic and coworkers used surface enhanced infrared reflection absorption spectroscopy (SEIRAS) whereas Dong et. al used shell-isolated nanoparticle-enhanced Raman spectroscopy (SHINERS) to investigate the reaction on the model single crystals of extended Au [31] and Pt [32,33] surfaces. Casalongue et. al conducted an in-situ x-ray photoelectron spectroscopy (XPS) at relatively low pressure (<100 Torr) [34] where humidified gas was used to simulate an aqueous electrolyte envi-

* Corresponding author at: Department of Chemical Engineering, University of Michigan, Ann Arbor, MI, USA.
E-mail address: linic@umich.edu (S. Linic).

https://doi.org/10.1016/j.jcat.2021.02.009
0021-9517/

ronment, while Nayak et. al used non-surface specific infrared spectroscopy to study Pt/C electrocatalysts in a limited vibrational mode range between 950 and 1500 cm^{-1}. [35] Due to these challenges in the spectroscopic characterization of electrochemical transformations, mechanistic understanding of ORR is largely based on either quantum chemical calculations (mainly employing Density Functional Theory (DFT)) of the energetics of various proposed reaction intermediates on idealized model Pt surfaces and on the experimental studies of reaction kinetics which are coupled to the mechanism using variations of micro-kinetic modelling [16].

Spectroscopic studies on non-model Pt nanoparticle electrocatalysts represent a missing link that would be very valuable, since it would serve to validate or dispute the mechanisms proposed based on the studies of model systems. In this work we present an in-operando spectroscopic study of the reaction intermediates involved in ORR on electrified Pt nanoparticle electrocatalysts. To accomplish this, we have designed and synthesized Ag-Pt core–shell nanoparticles, that contain a thin shell of Pt (approximately 1 nm) deposited on Ag nanoparticle cores (~60 nm diameter). We show that these nanostructures are ideal platforms for in-operando Plasmon Enhanced Raman Spectroscopy (PERS) of ORR on the Pt surface sites since the electrochemical transformations take place on the Pt surface, while the Ag core plays a role of an antenna which amplifies the Raman signal through the excited localized surface plasmons, giving us the required spectroscopic surface sensitivity. We combined these PERS studies with DFT calculations to assign the measured surface-specific Raman vibrational spectra to relevant surface intermediates as a function of electrocatalyst potential. This was done by using DFT calculations to compute vibrational fingerprints of likely surface intermediates at various potential-dependent Pt/electrolyte surface environments and identify the reaction intermediates that are consistent with the experimental spectra. These vibrational assignments were further verified and validated by performing PERS measurements in deoxygenated electrolyte and heavy oxygen (O_2-18) saturated electrolyte. These studies allowed us to identity the presence of critical reaction intermediates (OH, O_2, OOH, and H_2O) on the Pt surface as the function of operating voltage and derive voltage-dependent elementary step mechanisms of the reaction.

2. Synthesis and characterization of Ag-Pt core–shell nanoparticles:

We used a colloidal approach to synthesize the Ag-Pt core–shell nanostructures as described in detail in the methods section and previous publications [36,37]. In short, Ag nanoparticles of spherical shape with ~ 60 nm diameter were synthesized first. After washing, the Ag nanospheres were dispersed in a basic solution with a mild reducing agent (glucose). Upon addition of a Pt precursor (K_2PtCl_4), the Pt shell slowly forms on the Ag core. We have characterized these nanostructures, showing the presence of the thin Pt shell on the Ag cores. For example, the elemental mapping data in Fig. 1a shows a spherical core–shell nanoparticle of ~ 60 nm in diameter with a thin Pt shell surrounding Ag. Since cubical shapes are easier to characterize with scanning transmission electron microscopy, we also synthesized Ag-Pt core–shell nanocubes using a similar approach. Further characterization of these materials is shown in the supplement (Figure S1) [36,37], suggesting an approximately 1 nm thick (~5 to 6 layers of Pt atoms) shell on Ag.

The first questions we wanted to address was whether these Ag-Pt core–shell nanoparticles show electrochemical ORR activity that is consistent with the activities of Pt electrocatalysts. To address these questions, we used a three electrode rotating disk (RDE) setup to measure the ORR activity of the Ag-Pt core–shell nanostructures supported on carbon black in an O_2 saturated 0.1 M NaOH solution and compared it to the uncoated 60 nm Ag nanoparticle cores. The kinetic current densities (reaction rates) for the Ag-Pt and Ag nanoparticle electrocatalysts, measured at the voltage of 0.9 versus a reversible hydrogen electrode (RHE) and normalized to the respective electrochemically active surface area of the Ag and Pt using a RDE, are plotted in the inset in Fig. 1b [38,39]. The data in Figure S2 in the supplement show the electrochemical surface-area normalized kinetic current density over a range of applied voltages. The data in Fig. 1b insert and Figure S2 show that the kinetic current (reaction rate) on Ag-Pt core–shell nanoparticles electrocatalyst is ~ 7 times higher than the rate on the Ag nanoparticle electrocatalyst, suggesting that the Pt surface atoms in the Ag-Pt core–shell nanoparticles are performing the reaction. Furthermore, the data in Fig. 1b (insert) shows that the kinetic ORR current on the Ag-Pt core–shell nanoparticle electrocatalyst at 0.9 V vs. RHE is ~ 1.4 mA per cm^2 of Pt which is quantitatively consistent with the literature reported values for Pt nanoparticle electrocatalysts [40,41] and a polycrystalline-Pt electrode (Figure S3), suggesting that the electrochemical ORR takes place on the surface Pt sites which are engulfing the Ag core atoms.

We also assessed the ability of these Ag-Pt core–shell nanostructures to support surface enhancements in Raman spectroscopy measurements. The data in Fig. 1c show measured Raman spectra (obtained using a 532 nm Raman laser) of a probe dye molecule (methylene blue (MB)) deposited on three different substrates. The data show that for MB deposited on a silica chip and on pure Pt nanoparticles covering the Si chip, the MB Raman spectra is hardly detectable. On the other hand, for an identical MB concentration deposited on the Ag-Pt core–shell nanoparticle on the silica chip, the intensity of Raman scattering is larger by several orders of magnitude. The reason for this large Raman intensity enhancement is that the Ag core in the Ag-Pt core–shell nanoparticles interacts strongly with the incident 532 nm photons of the Raman laser through the excitation of localized surface plasmon resonance (LSPR). This strong interaction of light with the nanostructure results in an elevated optical extinction of the nanoparticles at resonant frequencies as shown in Fig. 1d. Under these resonant excitation conditions, strong oscillating electric fields are established at the surface of the nanoparticle, amplifying the rates of Raman surface scattering [42–44]. We used finite difference time domain (FDTD) optical modeling (see the supplement for details) to show that the oscillating electric field intensity is ~ 35 times larger around the Pt shell of a Ag-Pt nanoparticle (consistent with our nanoparticle geometry) compared to the electric field of incoming light (Figure S4). This means that the expected surface enhancement in the Raman signal of a surface intermediate residing on the Ag-Pt nanoparticle surface compared to the surface of monometallic Pt nanoparticles is ~ 35^2 (which is ~ 10^3). We note that pure Pt nanoparticles do not support these plasmon induced Raman surface enhancement [44,45]. As a side note, we point out that the LSPR extinction spectra in Fig. 1d show that the plasmon peak for Ag-Pt nanoparticles is slightly red-shifted and broader compared to pure Ag nanoparticles, which is fully consistent with the engulfment of the Ag core by a thin Pt shell [46–48]. Collectively, the data in Fig. 1 show that the Ag-Pt core–shell nanoparticles achieve the reaction rates that are consistent with the reaction taking place on Pt nanoparticles, and that these materials are excellent platforms for surface sensitive Raman spectroscopy.

3. Spectroscopic results and discussion

The PERS measurements were performed in an electrochemical flow cell specifically designed for in-operando Raman spectroscopy (Figure S5) [49]. The working electrode contained the Ag-Pt core–shell nanoparticle electrocatalysts uniformly coated on a 100 nm

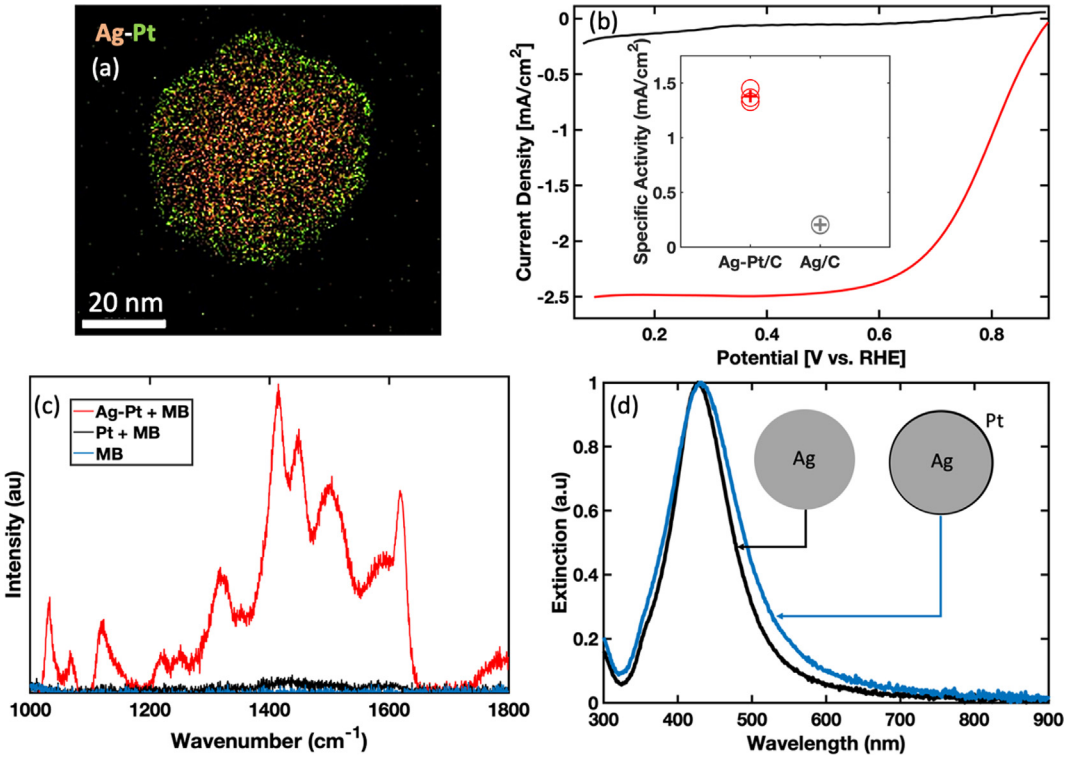

Fig. 1. (a) Energy-dispersive X-ray spectroscopy (EDS) map of the Ag-Pt nanoparticle. Ag is pink while Pt signal is green. (b) ORR current(rate)/voltage curve measured for the Ag-Pt nanoparticles at 50 mV/s in the in-operando flow cell in 0.1 M NaOH with O_2 (red) or He (black) saturating the electrolyte. (Inset) Electrochemical surface area normalized ORR current measured in a rotating disk electrode (RDE) setup of the Ag-Pt on carbon and monometallic Ag spheres on carbon. The kinetic current was measured at 0.9 V vs. RHE in O_2 saturated 0.1 M NaOH. (c) Raman spectra of methylene blue (MB) on a silica chip with and without the Ag-Pt nanoparticles or Pt nanoparticles (~20 nm diameter). The MB was deposited on the three substrates at identical concentration. The Raman laser wavelength was 532 nm. (d) UV–vis extinction spectra of the Ag nanoparticle (60 nm diameter) and the identical Ag particles covered by a thin Pt shell.

thick Ag film. We used Hg/HgO as a reference electrode and a clean Pt wire as a counter electrode. The data in Fig. 1b show that the current (reaction rate) as a function of applied potential measured on the Ag-Pt nanoparticle electrocatalysts in this flow cell system exhibits all the features consistent with the ORR electrochemistry on Pt, including the mass transport, polarization and kinetic limited ORR rate regimes. The Pt-surface normalized kinetic current is also consistent with the currents measured in the rotating disk setup discussed above.

The data in Fig. 2a show the measured vibrational Raman spectra as the function of voltage obtained for the Ag-Pt core–shell nanoparticles in the O_2–saturated (ORR taking place) and deoxygenated, He-saturated 0.1 M NaOH electrolyte. We note that the Raman spectra on the core–shell Ag-Pt nanoparticles look different than those measured on Ag nanoparticle cores (see Figure S6). The PERS data on Ag-Pt show three information-rich families of Raman spectra:

(i) The O_2 and the electrode potential-sensitive Raman modes, appearing at 933, 1072, 1102, 1131, 1404 and 1441 cm^{-1} (see Fig. 2a and 2b). These modes do not show up in the He-saturated electrolyte. The data in Fig. 2a show representative PER spectra, while the data in Fig. 2b shows the statistical analysis (detailed in Figure S7) of the intensities of the Raman peaks as the function of voltage. The data show that as the potential increases, the intensities of the O_2-sensitive bands of peaks at 933, 1072, 1102, 1131 and 1404 cm^{-1} increase. On the other hand, the intensity of the O_2-sensitive 1441 cm^{-1} mode decreases with increasing electrode potentials.

(ii) The Raman modes at 1600, 1664, 2020 cm^{-1} (see Fig. 3a and 3b) that appear with identical intensities in both, the O_2— and He-saturated electrolytes, and are sensitive to changes in the electrode potential. The data show that the voltage-dependent and oxygen-insensitive spectral features at 1600 cm^{-1} is maximized at 750 mV while the features at 1664 cm^{-1} and 2020 cm^{-1} decrease with increasing potential.

(iii) the Raman features between 2800 and 3000 cm^{-1} that exhibit a weak electrode potential dependence and that appear in the O_2— and He-saturated electrolytes. The data in Fig. 3a show that at a given potential the intensity of these modes is larger in the O_2-saturated compared to the He-saturated electrolytes.

To aid in the assignment of the experimentally measured Raman spectra, DFT calculations were used to model the complex, potential-dependent Pt/electrolyte(water) interface. We employed the Pt(111) model surface, which is consistent with the spherical shape of the nanoparticles used in the PERS measurements that are dominated by the (111) surface facet. Our strategy was to focus on the thermodynamically stable, potential-dependent geometric configurations of the Pt/water interface that have been derived previously based on ab-initio thermodynamics and molecular dynamics modeling [17,50]. The vibrational Raman spectra of the likely reaction intermediates (O_2, OH, O, OOH, etc.) was calculated by embedding these intermediates within these potential-dependent, thermodynamically relevant surface/water interfaces and converging the structures to their lowest energy configurations.

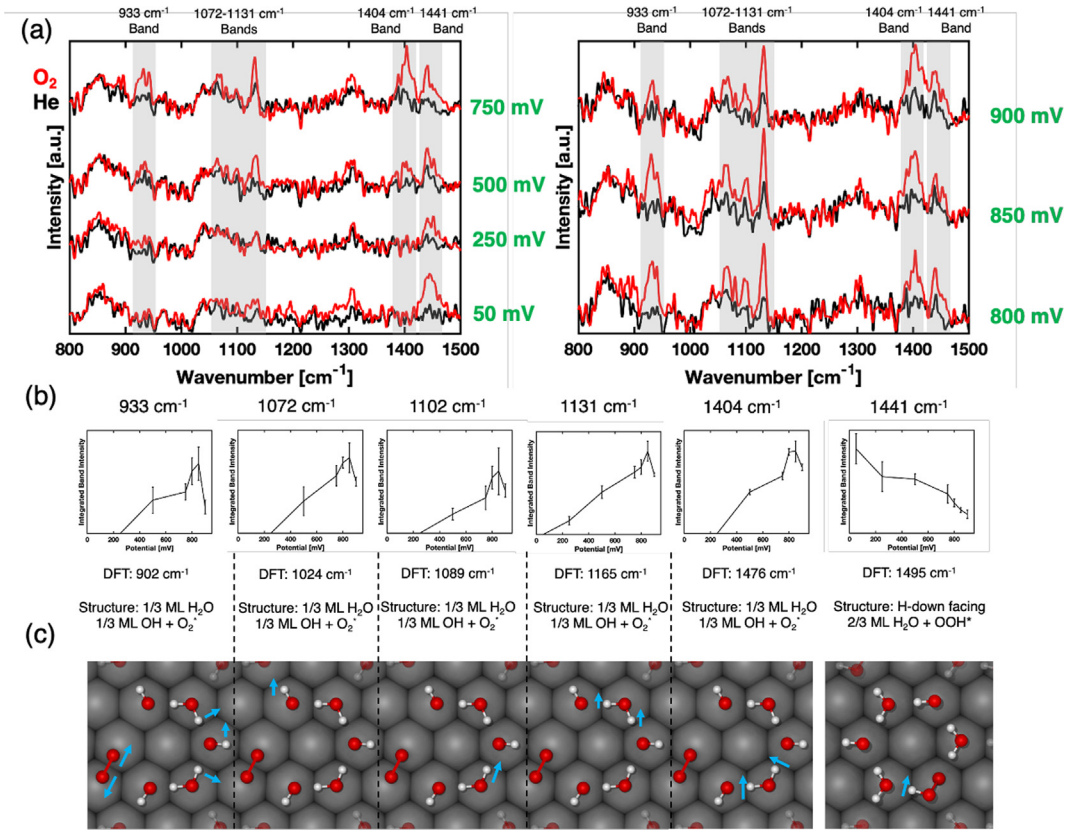

Fig. 2. (a) Measured in-operando PER spectra of Ag-Pt nanoparticles in O_2 and He saturated 0.1 M NaOH at electrode voltages from 50 to 900 mV vs. RHE. (b) Statistical analysis of potential dependent intensity changes for oxygen sensitive bands of peaks at 933, 1072, 1102, 1131, 1404, and 1441 cm^{-1}. Error bars are ± the standard error of the population mean of n spectra taken for each potential where n is a minimum of 3. (c) The arrows represent the DFT calculated movement of atoms corresponding to different Raman vibrational modes. The 3x3 surface unit cell was employed.

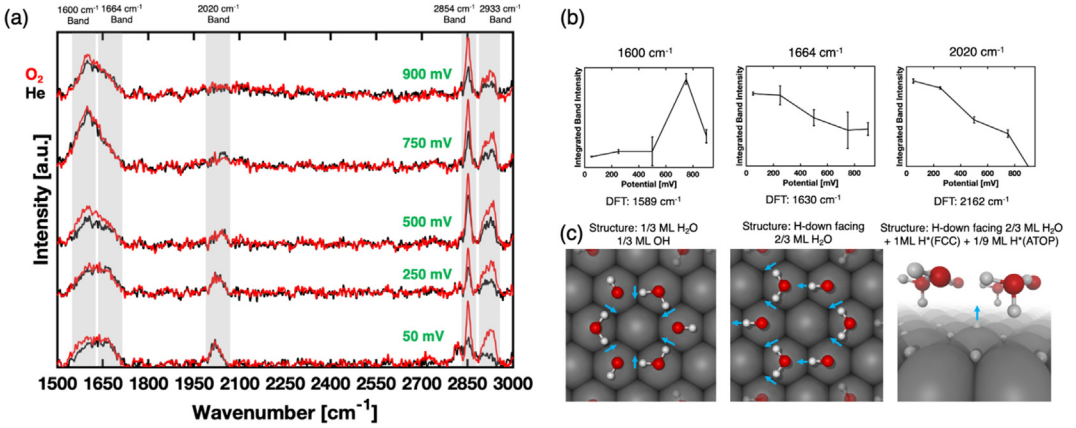

Fig. 3. (a) Measured in-operando PER spectra of Ag-Pt nanoparticles in O_2 and He saturated 0.1 M NaOH from 50 to 900 mV vs. RHE. (b) Statistical analysis of potential dependent intensity changes for oxygen insensitive modes at 1600, 1664 and 2020 cm^{-1}. Error bars are ± the standard error of the population mean of n spectra taken for each potential where n is a minimum of 3. (c) The arrows represent the DFT calculated movement of atoms corresponding to different Raman vibrational modes. The 3x3 surface unit cell was employed.

The relevant potential-dependent water/Pt(1 1 1) interfacial configurations are shown in Figure S8. At potentials below 450 mV wrt. RHE, the process of the hydrogen underpotential deposition on Pt takes place. Ab-initio thermodynamic studies have shown that under these conditions, a water layer with the water hydrogen atoms facing towards the surface rests above underpotential deposited hydrogen (H-UPD) atoms adsorbed in three-fold hollow sites (Figure S8a) [51,53]. As potential increases, the H-UPD atoms desorb from the surface, and the water layer above the Pt surface moves closer to the surface (Figure S8b). As potential further increases, the Pt surface approaches the potential of zero charge (pzc), allowing the water molecules to be more loosely arranged above the Pt surface [54]. Eventually, water molecules are split and the hydroxide adsorbate (OH) starts populating the surface above ~ 650 mV [17]. This leads to the formation of OH-H_2O hydrogen bonds which results in the establishment of the hydrogen bonding-reinforced hexagonal H_2O/OH network, which resides flat on the Pt surface (Figure S8c). At the electric potential

above ~ 650 mV two OH/H_2O networks are considered: (1) a 1/3ML-OH/1/3ML-H_2O and a (2) 5/12ML-OH/3/12MLH_2O. Both structures have similar free energy and both have been identified as thermodynamically stable under these conditions [17,50]. As potential increases further above 0.9 V, the O-H bond in the adsorbed OH is cleaved and oxygen atoms are formed on the Pt surface. We note that due to the diversity of surface sites on our non-model nanoparticle systems and dynamic fluctuations, there are significant overlaps between these different phases as a function of voltage.

As mentioned above, our approach was to embed various possible reaction intermediates (O_2, OOH, OH, O) in these thermodynamically stable water/Pt networks and use DFT to compute the Raman spectra associated with these intermediates. In this process, we identified the lowest energy states of the intermediates in these water/Pt networks, and by comparing the measured to the computed Raman spectra, we were able to identify the reaction intermediates as the function of potential.

We first focus on the analysis of the O_2 and electrode potential-sensitive spectral features at 933, 1072, 1102, 1131, 1404 cm^{-1}. The data in Fig. 2b show that these Raman bands increase in intensity as the function of the electrode potential. Based on the DFT calculations, we assigned these bands to the structures where an O_2 molecule is embedded in a 1/3ML-OH/1/3ML-H_2O structure [17]. Collective atomic movements associated with these Raman active vibrational modes are indicated by blue arrows in Fig. 2c. For example, the DFT simulated mode at 903 cm^{-1} (measured at 933 cm^{-1}) is directly associated with the O-O stretch within the O_2 molecule on the Pt surface embedded in the 1/3ML-OH/1/3ML-H_2O network, giving us an indication for the presence of this intermediate. The other modes are associated with the movements of atoms in this 1/3ML-OH/1/3ML-H_2O network, which are influenced by the presence of O_2 within the network. The intensity of these modes increases as the function of potential, which is consistent with the fact that the OH/H_2O network starts appearing on the surface at higher voltages as the OH adsorbate starts to populate the surface Pt sites. Another piece of information that supports these Raman mode assignments is that the modes associated with the motions of atoms in the flat OH/H_2O network (1072, 1102, 1131, 1404 cm^{-1}) are very weak or do not appear in the He-purged electrolyte (i.e., without the O_2 present in the electrolyte). The reason is that the Raman selection rules for the hexagonal symmetry of the 1/3ML-OH/1/3ML-H_2O network makes these modes Raman inactive. The introduction of O_2 to the surface leads to the breaking of the symmetry of the hexagonal network, which gives rise to these modes.

The data in Fig. 2b show that unlike the above discussed modes associated with the O_2 molecule on the surface, the intensity of the O_2-sensitive mode at 1441 cm^{-1} decreases with increasing potential. Based on DFT calculations, we assigned this peak to the OOH intermediate embedded in a network of 2/3 ML H_2O molecules with the H atoms in H_2O pointing to the Pt surface (Fig. 2c and Figure S8b). This H_2O structure is more stable at lower potentials owing to the negatively charged Pt surface that electrostatically reorients the water molecules toward this configuration. The decreasing intensity of the vibrational mode with increasing potential suggests that the surface concentration of the OOH intermediate declines as the function of an increasing voltage.

To further confirm the assignments of the modes between 933 and 1441 cm^{-1}, we performed Raman measurements when we replaced the O_2-16 reactant with the O_2-18 isotope. Quite surprisingly we found that these Raman modes were insensitive to the nature of the O_2 isotope (Figure S9). To explain this observation, we performed DFT calculations to compute the Raman spectra for O_2-16 and O_2-18 in vacuum (Figure S10) and in the thermodynamically stable interfacial structures. These calculations supported the experimental observations leading us to conclude that in this water environment, the O_2 isotopic labeling does not yield significant shifts in the observed Raman spectra associated with the O_2 intermediates due to the collective nature of the molecular vibrations (Table S1 and S2).

We also analyzed the potential-dependent behavior of the spectral features that are not sensitive to the presence of O_2 in the electrolyte and that appear with equal intensities in the O_2— and He-purged electrolyte (Fig. 3). The Raman band centered at 1600 cm^{-1} increases with increasing potential reaching its maximum intensity at 750 mV (Fig. 3b). Based in DFT calculations, we assign this peak to the H_2O bending mode in the 1/3ML-OH/1/3ML-H_2O network. The observed maximum intensity of this mode at the potential of around 750 – 800 mV is consistent with the notion that at the potentials higher than ~ 800 mV the H_2O/OH network is disrupted by the formation of the O atoms on the surface, while at significantly lower potentials the OH is not available on the surface. It is informative to note that unlike the above-discussed Raman inactive H_2O/OH modes (1072, 1102, 1131, 1404 cm^{-1}), which are not visible in the He electrolyte due to the hexagonal symmetry of the 1/3ML-OH/1/3ML-H_2O network on Pt, the mode at 1600 cm^{-1} can be detected in both electrolytes since it is not subject to the same Raman surface selection rules.

The data in Fig. 3a and b also show that the bands at 1664 cm^{-1} and 2020 cm^{-1} decrease in intensity as the potential is increased in both the He and O_2 electrolytes. Our DFT calculations show that the 1664 cm^{-1} mode corresponds to a molecular H_2O bending within the 2/3 ML H_2O structure with H atoms in water facing down to the Pt surface. We assigned the peak at 2020 cm^{-1} to the Pt-H vibrations, where H atoms in Pt top sites, surrounded with H_2O vibrate on the Pt surface. This H-vibration mode has also been previously identified in the literature to appear between 2000 and 2100 cm^{-1} [55]. It has also been proposed that this mode exhibits a strong Stark tuning effect, with its frequency changing with electric field intensity [51,52]. This Stark tuning effect is observed in our experimental data in Fig. 3 that show this mode shifts to higher wavenumbers as the potential is increased. We note that in this same vibrational range, in the CO-polluted electrolyte, a linearly bonded CO on Pt would appear. To rule out the potential interference of CO, we measured the Raman spectra for CO saturated electrolyte. Data in Figure S11 show that the CO adsorbed on the Pt sites of Ag-Pt core–shell nanoparticles exhibits different spectral features compared to those we assigned to H on Pt. [56] (see Figure S11 and supplement for further discussion).

Additionally, we also detected Raman modes centered at 2854 and 2933 cm^{-1} in both, the oxygen and helium saturated electrolytes. These modes are more intense when O_2 is present and do not exhibit significant potential dependence (Figure S12). These peaks match well with modes associated with the movement of H atoms in the 1/3ML-OH/1/3ML-H_2O (2835, 2879 cm^{-1}) and the 5/12ML-OH/3/12ML-H_2O structures (2853, 2980 cm^{-1}). Since these OH/H_2O networks are not stable on the Pt(1 1 1) surface at the low potentials (50, 250 mV), we cannot associate these modes with these surface networks. Potential explanation for these modes is that, as pointed by Janik and coworkers, these OH/H_2O networks can exist on more chemically active non–(1 1 1) surface facets of Pt even at low potentials (50, 250 mV) [57]. This would imply that these OH/H_2O networks could exist at low potentials on the Pt defects such as edges and kinks sites. Alternatively, these modes could simply be associated with the networks of OH^- surrounded with H_2O molecules in the vicinity or at the electrocatalyst surface. Since these modes are more pronounced when O_2 is present, this would indicate that the introduction of O_2 leads to an accumulation of OH^- at the surface within the double layer.

There are a few critical observations of the PERS studies that shed light on the reaction mechanism. First, the measured Raman

spectra directly identifies the potential-dependent, thermodynamically stable structures at the water/Pt electrified interface on Pt nanoparticle electrocatalysts. At low potentials, loosely bonded water molecules with hydrogens facing down populate the Pt surface. As the potential is increased, water and hydroxyl molecules are adsorbed more strongly on Pt top sites in a hexagonal 1/3ML-OH/1/3ML-H_2O surface patterns as evidenced by bands of peaks at 1072, 1102, 1131, 1404 and 1600 cm^{-1}. This structure seems to be the most pronounced at around 750 mV as OH and H_2O molecules are replaced with O atoms at higher voltages. Perhaps a surprising outcome of this work is that these different thermodynamically stable configurations seem to co-exist on the nanoparticle surface over relatively wide potential ranges, indicating that the diversity of the surface sites provides a wide range of binding energies for surface intermediates (mainly OH and O) that influence the existence of the different surface structures. Perhaps most importantly, our spectroscopic data point to the existence of surface intermediates with the preserved O—O chemical bond. The data showed that at high potentials, the O-O surface intermediate was observed (peak at 933 cm^{-1}). The data also show that at lower potentials the O—OH intermediate (peak at 1441 cm^{-1}) was detected which is consistent with the recent in-situ studies by Nayak et. al that showed decreasing abundance of OOH as a function of increasing potential [35]. These observations suggest that over a wide range of operating voltage, the oxygen reduction reaction could proceeds via an associative mechanism where O_2 does not spontaneously, thermally decompose on the Pt surface upon its adsorption.

The sketch in Fig. 4, shows the potential energy surface of the ORR on Pt surface sites that is consistent with the spectroscopic analysis reported herein. The potential-dependence of the relative abundance of these two intermediates (O-O and O-OH), where at high electrode potentials the O-O intermediate is detected at higher quantities, and at low potentials O-OH is a more abundant intermediate, is suggestive of the fact that the dissociation of O_2 involves a proton-electron addition to the adsorbed O_2 and the formation of the O-OH intermediate. At high voltages (Fig. 4), the proton-electron addition step (O_2^* + (e^- + H^+) →*OOH in acid and O_2^* + (e^- + H_2O) →*OOH + OH^- in base) is slow compared to the O-OH dissociation step, so we can observe the O-O intermediate on the surface. On the other hand, at lower voltages, the proton-electron addition step is fast, and the O-OH intermediate is trapped on the surface. The fact that we can even observe the O-OH intermediate leads us to conclude that the dissociation of this intermediate is an activated process with an activation barrier that is low but sufficient for the trapping of this intermediate on the surface. Finally, these spectroscopic studies support the notion that the Pt surface operates in two different kinetic regimes as a function of the Pt electrode potential. At high voltage, the reaction rate is affected by the presence of the packed network of OH and water, which makes it difficult for O_2 to find landing spots on the surface, and by the slow rates of proton-electron addition to the adsorbed O_2. On the other hand, at lower voltages (far from equilibrium) the surface is clean and the rate is controlled by the formation of the O-OH intermediate and its conversion to OH and O.

4. Conclusions

In-operando characterization of heterogeneous electrochemical reactions at the levels of elementary steps and critical surface intermediates is challenging due to a buried, complex and potential-dependent electrolyte/electrocatalyst interface where these reactions take place. To address this challenge, we have designed and synthesized Ag-Pt core–shell nanoparticle electrocatalysts that exhibits a high degree of surface enhancements in Raman spectroscopy. The Raman surface enhancements are derived from the Ag core which interacts strongly with visible light through the excitation of LSPR. This material platform allows us to study the (electro)chemical transformations that take place on Pt surfaces and probe surface intermediates with a high surface sensitivity. We note that monometallic Pt nanoparticles do not support surface enhancements in Raman spectroscopy. We have used these nanoparticle materials to perform a detailed Raman spectroscopy study of the mechanism of electrochemical ORR. The studies showed that these materials exhibit the ORR activity consistent with monometallic Pt electrocatalysis. Based on the DFT computed assignments of Raman spectral features we identified the critical electrolyte/Pt interfacial structures as a function of electrode voltage. Furthermore, the spectroscopic studies allowed us to identify the O-O and O-OH surface intermediates on the Pt surface, suggesting that the associative ORR mechanism plays a critical role over a wide range of potentials. The spectroscopic studies also revealed that the Pt surface operates in two different ORR kinetic regimes as a function of the operating potential. At high voltage, the reaction rate is affected by the presence of the network of adsorbed OH and water, which makes it difficult for O_2 to find landing sites on the surface, and by the slow rates of proton-electron addition to the adsorbed O_2. On the other hand, at lower voltages the surface is clean, and the rate is controlled by the formation of the O-OH intermediate and its conversion to OH and O.

5. Data Availability

The data that support the findings of this study are available from the corresponding author upon reasonable request.

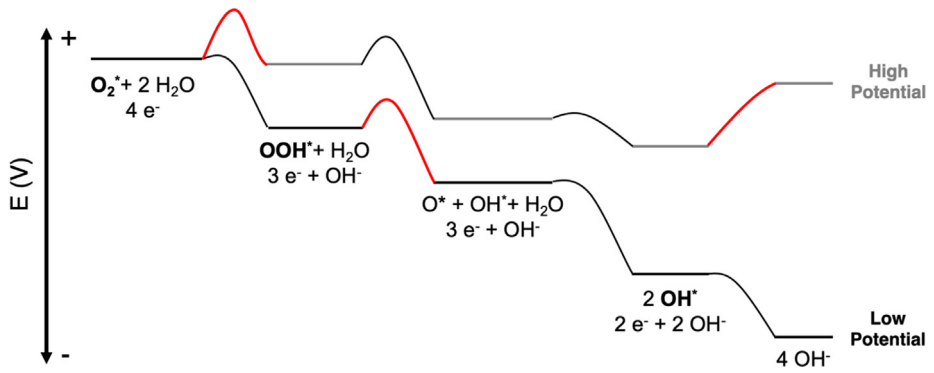

Fig. 4. Potential energy surface for various intermediates of the ORR on Pt derived from the PERS data. High potential is consistent with ~ 750–900 mV while low potential refers to ~ 50–500 mV. The red barriers indicate kinetically relevant steps that trap reactant intermediates on the Pt surface allowing for spectroscopic detection.

Declaration of Competing Interest

The authors declare that they have no known competing financial interests or personal relationships that could have appeared to influence the work reported in this paper.

Acknowledgments

This work was supported by the US DOE Office of Basic Energy Sciences, Division of Chemical Sciences (DE-SC0021008). The secondary support for the synthesis of core-shell nanostructures was provided by the National Science Foundation (NSF) (CBET-1702471 and CHE-1800197). The authors acknowledge technical support from the Michigan Center for Materials Characterization (MC^2). The authors also thank Dr. Umar Aslam, Dr. Ali Motagamwala and Steven Chavez for important discussions and technical knowledge.

Appendix A. Supplementary material

Supplementary data to this article can be found online at https://doi.org/10.1016/j.jcat.2021.02.008.

References

[1] Fuel Cells | Department of Energy https://energy.gov/eere/fuelcells/fuel-cells (accessed Jun 20, 2018).
[2] T. Yoshida, K. Kojima, Toyota MIRAI Fuel Cell Vehicle and Progress Toward a Future Hydrogen Society, Electrochem. Soc. Interf. 24 (2) (2015) 45–49, https://doi.org/10.1149/2.F03152if.
[3] U.S. Energy Information Administration (EIA) - Total Energy Monthly Data https://www.eia.gov/totalenergy/data/monthly/ (accessed Mar 28, 2019).
[4] J.K. Nørskov, J. Rossmeisl, A. Logadottir, L. Lindqvist, J.R. Kitchin, T. Bligaard, H. Jónsson, Origin of the Overpotential for Oxygen Reduction at a Fuel-Cell Cathode, J. Phys. Chem. B 108 (46) (2004) 17886–17892, https://doi.org/10.1021/jp047349j.
[5] Z.P. Cano, D. Banham, S. Ye, A. Hintennach, J. Lu, M. Fowler, Z. Chen, Batteries and Fuel Cells for Emerging Electric Vehicle Markets, Nat. Energy 3 (4) (2018) 279, https://doi.org/10.1038/s41560-018-0108-1.
[6] M. Luo, Y. Sun, X. Zhang, Y. Qin, M. Li, Y. Li, C. Li, Y. Yang, L. Wang, P. Gao, G. Lu, S. Guo, Stable High-Index Faceted Pt Skin on Zigzag-Like PtFe Nanowires Enhances Oxygen Reduction Catalysis, Adv. Mater. (2018), https://doi.org/10.1002/adma.201705515.
[7] T.V. Cleve, S. Moniri, G. Belok, K.L. More, S. Linic, Nanoscale Engineering of Efficient Oxygen Reduction Electrocatalysts by Tailoring the Local Chemical Environment of Pt Surface Sites, ACS Catal. 7 (1) (2017) 17–24, https://doi.org/10.1021/acscatal.6b01565.
[8] H. Xin, A. Holewinski, S. Linic, Predictive Structure-Reactivity Models for Rapid Screening of Pt-Based Multimetallic Electrocatalysts for the Oxygen Reduction Reaction, ACS Catal. 2 (1) (2012) 12–16, https://doi.org/10.1021/cs200462f.
[9] J. Huang, M. Eikerling, Modeling the Oxygen Reduction Reaction at Platinum: A Brief Review of Recent Developments, Current Opin. Electrochem. (2019), https://doi.org/10.1016/j.coelec.2019.01.004.
[10] X. Huang, Z. Zhao, L. Cao, Y. Chen, E. Zhu, Z. Lin, M. Li, A. Yan, A. Zettl, Y.M. Wang, X. Duan, T. Mueller, Y. Huang, High-Performance Transition Metal-Doped Pt3Ni Octahedra for Oxygen Reduction Reaction, Science 348 (6240) (2015) 1230–1234, https://doi.org/10.1126/science.aaa8765.
[11] G.-R. Zhang, S. Wöllner, Hollowed Structured PtNi Bifunctional Electrocatalyst with Record Low Total Overpotential for Oxygen Reduction and Oxygen Evolution Reactions, Appl. Catal. B: Environ. 222 (Supplement C) (2018) 26–34, https://doi.org/10.1016/j.apcatb.2017.09.066.
[12] C. Wang, L. Zhang, H. Yang, J. Pan, J. Liu, C. Dotse, Y. Luan, R. Gao, C. Lin, J. Zhang, J.P. Kilcrease, X. Wen, S. Zou, J. Fang, High-Indexed Pt3Ni Alloy Tetrahexahedral Nanoframes Evolved through Preferential CO Etching, Nano Lett. 17 (4) (2017) 2204–2210, https://doi.org/10.1021/acs.nanolett.6b04731.
[13] C. Chen, Y. Kang, Z. Huo, Z. Zhu, W. Huang, H.L. Xin, J.D. Snyder, D. Li, J.A. Herron, M. Mavrikakis, M. Chi, K.L. More, Y. Li, N.M. Markovic, G.A. Somorjai, P. Yang, V.R. Stamenkovic, Highly Crystalline Multimetallic Nanoframes with Three-Dimensional Electrocatalytic Surfaces, Science 343 (6177) (2014) 1339–1343, https://doi.org/10.1126/science.1249061.
[14] K.D. Jensen, J. Tymoczko, J. Rossmeisl, A.S. Bandarenka, I. Chorkendorff, M. Escudero-Escribano, I.E.L. Stephens, Elucidation of the Oxygen Reduction Volcano in Alkaline Media Using a Copper–Platinum(111) Alloy, Angew. Chem. Int. Ed. 57 (11) (2018) 2800–2805, https://doi.org/10.1002/anie.201711858.
[15] D. Wang, H.L. Xin, R. Hovden, H. Wang, Y. Yu, D.A. Muller, F.J. DiSalvo, H.D. Abruña, Structurally Ordered Intermetallic Platinum-Cobalt Core–Shell Nanoparticles with Enhanced Activity and Stability as Oxygen Reduction Electrocatalysts, Nat. Mater. 12 (1) (2013) 81–87, https://doi.org/10.1038/nmat3458.
[16] A. Holewinski, S. Linic, Elementary Mechanisms in Electrocatalysis: Revisiting the ORR Tafel Slope, J. Electrochem. Soc. 159 (11) (2012) H864–H870, https://doi.org/10.1149/2.022211jes.
[17] V. Tripkovic, T. Vegge, Potential- and Rate-Determining Step for Oxygen Reduction on Pt(111), J. Phys. Chem. C 121 (48) (2017) 26785–26793, https://doi.org/10.1021/acs.jpcc.7b07472.
[18] A. Gómez-Marín, J. Feliu, T. Edson, Reaction Mechanism for Oxygen Reduction on Platinum: Existence of a Fast Initial Chemical Step and a Soluble Species Different from H2O2, ACS Catal. (2018) 7931–7943, https://doi.org/10.1021/acscatal.8b01291.
[19] N. Ramaswamy, S. Mukerjee, Fundamental Mechanistic Understanding of Electrocatalysis of Oxygen Reduction on Pt and Non-Pt Surfaces: Acid versus Alkaline Media, Adv. Phys. Chem. 2012 (2012), https://doi.org/10.1155/2012/491604 e491604.
[20] B. Jayasankar, K. Karan, O2 Electrochemistry on Pt: A Unified Multi-Step Model for Oxygen Reduction and Oxide Growth, Electrochim. Acta 273 (2018) 367–378, https://doi.org/10.1016/j.electacta.2018.03.191.
[21] J. Huang, J. Zhang, M. Eikerling, Unifying Theoretical Framework for Deciphering the Oxygen Reduction Reaction on Platinum, PCCP (2018), https://doi.org/10.1039/C8CP01315B.
[22] N. Markovic, H. Gasteiger, P.N. Ross, Kinetics of Oxygen Reduction on Pt(Hkl) Electrodes: Implications for the Crystallite Size Effect with Supported Pt Electrocatalysts, J. Electrochem. Soc. 144 (5) (1997) 1591–1597, https://doi.org/10.1149/1.1837646.
[23] S. Sui, X. Wang, X. Zhou, Y. Su, S. Riffat, C. Liu, A Comprehensive Review of Pt Electrocatalysts for the Oxygen Reduction Reaction: Nanostructure, Activity, Mechanism and Carbon Support in PEM Fuel Cells, J. Mater. Chem. A 5 (5) (2017) 1808–1825, https://doi.org/10.1039/C6TA08580F.
[24] J.A. Gauthier, S. Ringe, C.F. Dickens, A. Garza, A.T. Bell, M. Head-Gordon, J.K. Norskov, K. Chan, Challenges in Modeling Electrochemical Reaction Energetics with Polarizable Continuum Models, ACS Catal. (2018), https://doi.org/10.1021/acscatal.8b02793.
[25] A.P. Sandoval-Rojas, A.M. Gómez-Marín, M.F. Suárez-Herrera, V. Climent, J.M. Feliu, Role of the Interfacial Water Structure on Electrocatalysis: Oxygen Reduction on Pt(1 1 1) in Methanesulfonic Acid, Catal. Today 262 (2016) 95–99, https://doi.org/10.1016/j.cattod.2015.08.046.
[26] F. Che, J.T. Gray, S. Ha, N. Kruse, S.L. Scott, J.-S. McEwen, Elucidating the Roles of Electric Fields in Catalysis: A Perspective, ACS Catal. (2018) 5153–5174, https://doi.org/10.1021/acscatal.7b02899.
[27] M.J. Eslamibidgoli, M.H. Eikerling, Approaching the Self-Consistency Challenge of Electrocatalysis with Theory and Computation, Curr. Opin. Electrochem. (2018), https://doi.org/10.1016/j.coelec.2018.03.038.
[28] R. Sundararaman, W.A. Goddard, T.A. Arias, Grand Canonical Electronic Density-Functional Theory: Algorithms and Applications to Electrochemistry, J. Chem. Phys. 146 (11) (2017), https://doi.org/10.1063/1.4978411 114104.
[29] V.R. Stamenkovic, D. Strmcnik, P.P. Lopes, N.M. Markovic, Energy and Fuels from Electrochemical Interfaces, Nat. Mater. 16 (1) (2017) 57, https://doi.org/10.1038/nmat4738.
[30] Kunimatsu, K.; Yoda, T.; A. Tryk, D.; Uchida, H.; Watanabe, M. In Situ ATR-FTIR Study of Oxygen Reduction at the Pt / Nafion Interface. Physical Chemistry Chemical Physics 2010, 12 (3), 621–629. https://doi.org/10.1039/B917306D.
[31] M.H. Shao, R.R. Adzic, Spectroscopic Identification of the Reaction Intermediates in Oxygen Reduction on Gold in Alkaline Solutions, J. Phys. Chem. B 109 (35) (2005) 16563–16566, https://doi.org/10.1021/jp053450s.
[32] M. Shao, P. Liu, R.R. Adzic, Superoxide Anion Is the Intermediate in the Oxygen Reduction Reaction on Platinum Electrodes, J. Am. Chem. Soc. 128 (23) (2006) 7408–7409, https://doi.org/10.1021/ja061246s.
[33] J.-C. Dong, X.-G. Zhang, V. Briega-Martos, X. Jin, J. Yang, S. Chen, Z.-L. Yang, D.-Y. Wu, J.M. Feliu, C.T. Williams, Z.-Q. Tian, J.-F. Li, In Situ Raman Spectroscopic Evidence for Oxygen Reduction Reaction Intermediates at Platinum Single-Crystal Surfaces, Nat. Energy 1 (2018), https://doi.org/10.1038/s41560-018-0292-z.
[34] H.S. Casalongue, S. Kaya, V. Viswanathan, D.J. Miller, D. Friebel, H.A. Hansen, J. K. Nørskov, A. Nilsson, H. Ogasawara, Direct Observation of the Oxygenated Species during Oxygen Reduction on a Platinum Fuel Cell Cathode, Nat. Commun. 4 (2013) 2817, https://doi.org/10.1038/ncomms3817.
[35] S. Nayak, I.J. McPherson, K.A. Vincent, Adsorbed Intermediates in Oxygen Reduction on Platinum Nanoparticles Observed by In Situ IR Spectroscopy, Angew. Chem. Int. Ed. 57 (39) (2018) 12855–12858, https://doi.org/10.1002/anie.201804978.
[36] U. Aslam, S. Linic, Addressing Challenges and Scalability in the Synthesis of Thin Uniform Metal Shells on Large Metal Nanoparticle Cores: Case Study of Ag–Pt Core-Shell Nanocubes, ACS Appl. Mater. Interf. 9 (49) (2017) 43127–43132, https://doi.org/10.1021/acsami.7b14474.
[37] U. Aslam, S. Chavez, S. Linic, Controlling Energy Flow in Multimetallic Nanostructures for Plasmonic Catalysis, Nat. Nanotechnol. 12 (10) (2017) 1000–1005, https://doi.org/10.1038/nnano.2017.131.
[38] J.G. Chen, C.W. Jones, S. Linic, V.R. Stamenkovic, Best Practices in Pursuit of Topics in Heterogeneous Electrocatalysis, ACS Catal. 7 (9) (2017) 6392–6393, https://doi.org/10.1021/acscatal.7b02839.
[39] S. Moniri, T. Van Cleve, S. Linic, Pitfalls and Best Practices in Measurements of the Electrochemical Surface Area of Platinum-Based Nanostructured Electrocatalysts, J. Catal. 345 (2017) 1–10, https://doi.org/10.1016/j.jcat.2016.11.018.

[40] M. Nesselberger, S. Ashton, J.C. Meier, I. Katsounaros, K.J.J. Mayrhofer, M. Arenz, The Particle Size Effect on the Oxygen Reduction Reaction Activity of Pt Catalysts: Influence of Electrolyte and Relation to Single Crystal Models, J. Am. Chem. Soc. 133 (43) (2011) 17428–17433, https://doi.org/10.1021/ja207016u.
[41] F.J. Perez-Alonso, D.N. McCarthy, A. Nierhoff, P. Hernandez-Fernandez, C. Strebel, I.E.L. Stephens, J.H. Nielsen, I. Chorkendorff, The Effect of Size on the Oxygen Electroreduction Activity of Mass-Selected Platinum Nanoparticles, Angew. Chem. Int. Ed. 51 (19) (2012) 4641–4643, https://doi.org/10.1002/anie.201200586.
[42] A. Marimuthu, P. Christopher, S. Linic, Design of Plasmonic Platforms for Selective Molecular Sensing Based on Surface-Enhanced Raman Spectroscopy, J. Phys. Chem. C 116 (17) (2012) 9824–9829, https://doi.org/10.1021/jp301443y.
[43] C. Boerigter, R. Campana, M. Morabito, S. Linic, Evidence and Implications of Direct Charge Excitation as the Dominant Mechanism in Plasmon-Mediated Photocatalysis, Nat. Commun. 7 (2016) 10545, https://doi.org/10.1038/ncomms10545.
[44] C. Boerigter, U. Aslam, S. Linic, Mechanism of Charge Transfer from Plasmonic Nanostructures to Chemically Attached Materials, ACS Nano 10 (6) (2016) 6108–6115, https://doi.org/10.1021/acsnano.6b01846.
[45] V.G. Rao, U. Aslam, S. Linic, Chemical Requirement for Extracting Energetic Charge Carriers from Plasmonic Metal Nanoparticles to Perform Electron-Transfer Reactions, J. Am. Chem. Soc. 141 (1) (2019) 643–647, https://doi.org/10.1021/jacs.8b11949.
[46] U. Aslam, V.G. Rao, S. Chavez, S. Linic, Catalytic Conversion of Solar to Chemical Energy on Plasmonic Metal Nanostructures, Nat. Catal. 1 (9) (2018) 656, https://doi.org/10.1038/s41929-018-0138-x.
[47] S. Chavez, U. Aslam, S. Linic, Design Principles for Directing Energy and Energetic Charge Flow in Multicomponent Plasmonic Nanostructures, ACS Energy Lett. (2018) 1590–1596, https://doi.org/10.1021/acsenergylett.8b00841.
[48] U. Aslam, S. Linic, Kinetic Trapping of Immiscible Metal Atoms into Bimetallic Nanoparticles through Plasmonic Visible Light-Mediated Reduction of a Bimetallic Oxide Precursor: Case Study of Ag–Pt Nanoparticle Synthesis, Chem. Mater. 28 (22) (2016) 8289–8295, https://doi.org/10.1021/acs.chemmater.6b03381.
[49] Redox.me. Magnetic Mount Raman Electrochemical Flow Cell https://redox.me/collections/spectro-electrochemical-cells/products/raman-efc-4-mm-path-0-7-ml-raman-electrochemical-flow-cell.
[50] M. Hangaard Hansen, A. Nilsson, J. Rossmeisl, Modelling PH and Potential in Dynamic Structures of the Water/Pt(111) Interface on the Atomic Scale, PCCP 19 (34) (2017) 23505–23514, https://doi.org/10.1039/C7CP03576D.
[51] E. Skúlason, G.S. Karlberg, J. Rossmeisl, T. Bligaard, J. Greeley, H. Jónsson, J.K. Nørskov, Density Functional Theory Calculations for the Hydrogen Evolution Reaction in an Electrochemical Double Layer on the Pt(111) Electrode, Phys. Chem. Chem. Phys. 9 (25) (2007) 3241–3250, https://doi.org/10.1039/B700099E.
[52] M. Tomonari, O. Sugino, DFT Calculation of Vibrational Frequency of Hydrogen Atoms on Pt Electrodes: Analysis of the Electric Field Dependence of the Pt–H Stretching Frequency, Chem. Phys. Lett. 437 (4) (2007) 170–175, https://doi.org/10.1016/j.cplett.2007.02.022.
[53] K. Kunimatsu, T. Senzaki, M. Tsushima, M. Osawa, A Combined Surface-Enhanced Infrared and Electrochemical Kinetics Study of Hydrogen Adsorption and Evolution on a Pt Electrode, Chem. Phys. Lett. 401 (4) (2005) 451–454, https://doi.org/10.1016/j.cplett.2004.11.100.
[54] R. Rizo, E. Sitta, E. Herrero, V. Climent, J.M. Feliu, Towards the Understanding of the Interfacial PH Scale at Pt(111) Electrodes, Electrochim. Acta 162 (2015) 138–145, https://doi.org/10.1016/j.electacta.2015.01.069.
[55] S. Zhu, X. Qin, Y. Yao, M. Shao, PH-Dependent Hydrogen and Water Binding Energies on Platinum Surfaces as Directly Probed through Surface-Enhanced Infrared Absorption Spectroscopy, J. Am. Chem. Soc. (2020), https://doi.org/10.1021/jacs.0c01104.
[56] K. Kunimatsu, T. Sato, H. Uchida, M. Watanabe, Role of Terrace/Step Edge Sites in CO Adsorption/Oxidation on a Polycrystalline Pt Electrode Studied by in Situ ATR-FTIR Method, Electrochim. Acta 53 (21) (2008) 6104–6110, https://doi.org/10.1016/j.electacta.2008.03.046.
[57] M.J. Janik, I.T. McCrum, M.T.M. Koper, On the Presence of Surface Bound Hydroxyl Species on Polycrystalline Pt Electrodes in the "Hydrogen Potential Region" (0–0.4 V-RHE), J. Catal. 367 (2018) 332–337, https://doi.org/10.1016/j.jcat.2018.09.031.